

Chapter 1

Acceleration-Sensitive Interference

This chapter describes the work towards realising an atom interferometer and subsequently measuring accelerations.

1.1 Chapter Outline

To-Do:

- Raman spectrum, identifying each transition
- Characterisation of velocity-selective pulse and each interferometer pulse using Rabi oscillations.
- Making a three-pulse atom interferometer
- Improving acceleration sensitivity and correlating vibrations using MEMS

1.2 Wavefront Requirements

1.3 Raman Optical System

When designing an optical system for the light used in an atom interferometer, it is worth paying attention to both the spatial extent and beam waist of the collimated beam. These requirements are particularly important in this experiment, where acceleration due to gravity is perpendicular to the Raman beam axis and causes significant transverse motion of the atoms. Firstly, the optical system must be designed to make sure that the atoms are illuminated by each interferometer pulse. In addition to this, a more subtle requirement on the fringe contrast constrains the beam waist size. The gradient of intensity across the atom cloud must be small so that each atom is driven by (approximately) the same Rabi frequency. Otherwise, this variation in the Rabi frequency will dephase the atoms, which reduces the interferometer fringe contrast.

A further constraint on the optical system comes from the effect of thickness variation of optical elements. If the optical path length of the light as it passes through an element is not uniform, this will lead to wavefront aberrations. A spatially-varying phase leads to a bias in the interferometer phase since it does not depend on acceleration. Moreover, since this phase is not the same for each atom, it is another source of dephasing. Considering the effects of wavefront aberrations was a large motivating factor for designing an optical system for use inside the vacuum chamber. Specifically, the distortions of a laser wavefront through optical viewports would drastically reduce the fringe contrast under transverse motion of the atoms during the interferometer. The process used to bond an optical viewport to a flange stresses the glass and distorts its thickness, producing wavefront aberrations that factor into the phase uncertainty

of an atom interferometer [Schkolnik2015]. **Add requirements on other optics**

1.3.1 Fringe Contrast Dependence

The effects of a gradient of intensity on the fringe contrast can be shown by considering an ensemble of atoms that are spatially distributed by a Gaussian distribution. Neglecting the effect of the ensemble's velocity distribution on the Raman detuning and for fixed pulse times, the pulse area $\Omega\tau$ varies only as a function of the radial displacement from the optic axis. The total fringe contrast can be determined by a convolution of the contrast for a single atom with the atomic density

$$\mathcal{C} = \int \frac{1}{\sqrt{2\pi}\sigma_c} e^{-r^2/(2\sigma_c^2)} f_{\pi/2-\pi-\pi/2}(\Omega(r-r_1), \Omega(r-r_2), \Omega(r-r_3)) \, dr \quad (1.1)$$

where σ_c is the radial width of the atom cloud, $f_{\pi/2-\pi-\pi/2}$ is the fringe contrast as previously described in equation (??) and r_i is the position of the ensemble's centre-of-mass at the i -th pulse. If the atom cloud is initially at the centre of the laser and falling under gravity, then these coordinates are $(0, -\frac{1}{2}gT^2, -2gT^2)$ respectively. Under the assumption that the two lasers which drive the Raman transition have the same waist size, the Rabi frequency, which is determined by the product of the electric fields (see equation (??)), can be described by

$$\Omega(r) = \Omega_0 e^{-2r^2/w^2} \quad (1.2)$$

where Ω_0 is the Rabi frequency along the optic axis and w is the waist size – the distance at which the electric field falls to $1/e$ of its peak value. The fringe contrast as a function as beam waist for an atom cloud of width a width $\sigma_c = 5$ mm and a time

between interferometer pulses of $T = 25$ ms is plotted in Figure 1.1. For small beam waists, the intensity gradient across the cloud significantly reduces the fringe contrast. In fact, a beam waist much greater than the width of the cloud is necessary to achieve a large contrast between the two interferometer states. Relaxing the assumptions made on the ensemble's velocity distribution to include its influence on the detuning and spatial distribution of the atoms during the interferometer would strengthen this argument.

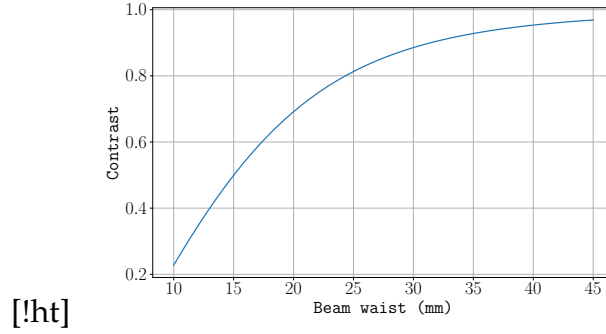


Figure 1.1: Simulated fringe contrast as a function of waist size w for an atom cloud falling under gravity. This model assumes a Gaussian distributed atomic density with a width $\sigma_c = 5$ mm and a time between interferometer pulses of $T = 25$ ms. For smaller beam waists the subsequent interferometer pulses have a larger intensity gradient across the atom ensemble, which increases the dephasing of the two states and reduces the interferometer fringe contrast.

So far, it has been shown that a large beam waist is necessary to achieve a high fringe contrast when allowing for transverse motion of the atoms across the laser wavefront. Otherwise, if the fringe contrast was poor, this would limit the sensitivity of the interferometer to accelerations rather than other effects which are less rectifiable. Another optical effect which influences the sensitivity is distortions of the laser wavefront. In an ideal case, the superposition of the spherical wavefronts of the two lasers results in a planar wavefront for the effective field which drives the Raman transition. However, propagation through rough optical elements distort these wavefronts and introduce a spatially varying component of the Raman phase that is independent of

acceleration. If the atom cloud's trajectory is parallel with the Raman axis, then this additional phase is the same at each laser pulse and is therefore cancelled out. Of course, this does not occur when the cloud moves transverse to the Raman axis where this random phase has the effect of reducing the fringe contrast. Starting with the assumption that this phase is Gaussian distributed around 0, with a standard deviation of σ_ϕ , if this is uncorrelated at each interferometer pulse, then the interferometer phase $\Delta\Phi$ will be distributed with a standard deviation of $\sigma_\Phi = \sqrt{6}\sigma_\phi$. Denoting this random phase as $\delta\phi$, the fringe contrast is then given by

$$\mathcal{C}(\delta\phi) = \cos(2\delta\phi) \quad (1.3)$$

Following from this, if $\delta\phi$ is uncorrelated between each atom, the expected value of the contrast over the ensemble is given by

$$\langle \mathcal{C} \rangle = \frac{1}{\sqrt{2\pi}\sigma_\Phi} \int \mathcal{C}(\delta\phi) e^{-\delta\phi^2/2\sigma_\Phi^2} d\delta\phi \quad (1.4)$$

$$= e^{-2\sigma_\Phi^2} \quad (1.5)$$

The value of this expected contrast is plotted in Figure 1.2 and shows a strong dependence on σ_ϕ .

Add more justification here. Cite Achim Peter's paper

1.3.2 Raman Beam Collimator

The optical system used to produce the beams for driving Raman transitions, which will conventionally be referred to as the Raman optics, was designed to reduce the previously mentioned effects which result in poorer interferometric fringe visibility and sensitivity to accelerations. Principally, the entire optical system was mounted

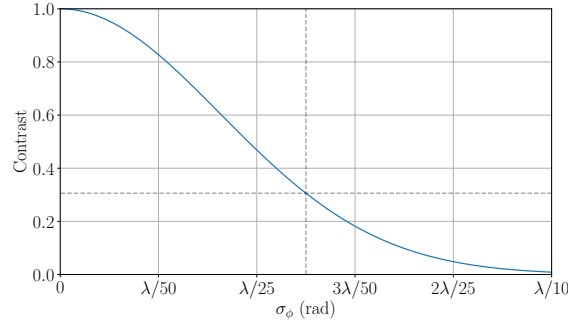


Figure 1.2: Expected contrast as a function of random phase contributions. This assumes that the phase imprinted on an atom during each interferometer pulse has an additional random component that is Gaussian distributed around 0 with a standard deviation of σ_ϕ . This random phase is also uncorrelated between each pulse so that the total can be obtained using Gaussian propagation of error. The dashed lines indicate the contrast for phase noise expected from conventional optics, which are usually engineered to a surface flatness of $\lambda/20$.

inside the optical chamber so that the Raman light does not pass through any optical viewports before interacting with the atoms. Typically, the stress placed on the glass during the bonding process will distort the flatness more than is acceptable for achieving a high contrast. For example the viewports used for the **mot!** (**mot!**) optics have a specified flatness of $\lambda/4$, so mounting the entire optical system inside the chamber was the simplest way to avoid a large distortion.

Figure 1.3a presents a diagram of the components used to send Raman light into the chamber and produce a collimated beam in the centre of the chamber. The light is coupled into the chamber using a UHV compatible **pm!** (**pm!**) fibre, manufactured by Diamond photonics. This is a kapton-coated PM-780 HP fibre that is bonded on one end to a DN16 flange using an epoxy resin. The external side of this flange has an FC/APC connector for coupling light from another fibre. Inside the chamber, the ferrule is connected to an FC/APC fibre plate. This is clamped between a piece which bolts onto the inside of a DN63 flange and another stainless steel plate which bolts onto the rest of the optics assembly. Fine adjustment of the position of the fibre along the optic axis is achieved using shim plates with a thickness ranging from

200–300 μm . The fibre plate is free to rotate so that the orientation of the fibre with respect to a **qwp!** (**qwp!**) at the output of the collimator. This **qwp!** is manufactured by Light Machinery, and is described further in Section 1.3.3. When the fibre is correctly orientated (e.g. when the slow axis of the fibre is at 45deg to the slow axis of the waveplate), the two Raman light fields are orthogonally circularly polarised.

The original design for the optical system consisted of a triplet lens, as a system of three lenses is capable of correcting for the five types of Seidel aberrations that distort rays of monochromatic light. This was designed and manufactured by IC Optical Systems. Another specification for this lens system was that it had to produce a collimated beam with a waist size of around 35 mm so that the sensitivity of the interferometer was not limited by the effects of intensity gradients across the atoms. Unfortunately, the triplet was designed with an incorrect **na!** (**na!**). With a focal length of 123.4 mm and a diameter of 50 mm, the triplet lens has a **na!** of 0.194. However, the nominal **na!** for PM780-HP fibre used in the UHV compatible **pm!** fibre is 0.12. Consequently, the light from this fibre did not fill the **na!** of the triplet lens and produced a beam with a waist of 13mm. **Plot to illustrate this.** To address this issue, a pair of aspheric lenses was included to increase the divergence angle of light from the fibre. These are manufactured by Thorlabs and have a focal length of 4.51 mm (352230-B) and 15.29 mm (352260-B), respectively, to give a magnification of 3.39.

Alignment and Collimation

As one of the main motivations for mounting the Raman optics inside the vacuum chamber was to reduce the effects of wavefront distortions, it is worth highlighting how inaccurate alignment of the optics can lead to aberrations. As discussed before (see Section 1.3.1), distortions of the wavefront leads to a dephasing and loss of interferometer fringe visibility. Here, the same figures of merit as before are used

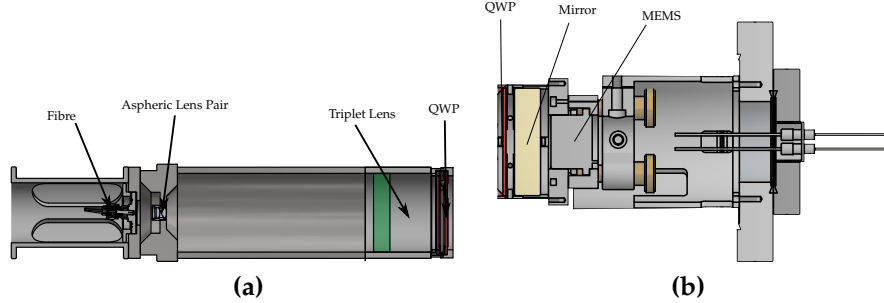


Figure 1.3: Diagrams of the components used in the Raman optical assemblies. (a) shows the collimator setup. Light is coupled into the chamber using a UHV fibre feedthrough. A pair of aspheric lenses is used to increase the divergence angle of the fibre output, before the light is collimated by a triplet lens. Finally, a quarter-wave plate is aligned so that it circularly polarises the collimated light fields. (b) illustrates the other half of the setup, which is used to retro-reflect the light. A second quarter-wave plate is used so that the reflected beams have the same handedness to their respected incoming ones. A MEMS accelerometer is mounted on the back of the mirror to measure vibrations. These components are all mounted on a piezo-controlled mirror mount whose tilt can be controlled from outside the vacuum chamber.

to consider what misalignment is acceptable to ensure that the phase of the Raman wavefront deviates by less than $\lambda/100$ after a transverse distance of 12.5 mm.

Taking the fibre as a point source, misalignment can occur if it is displaced from the front focal point of the optical system longitudinally along or transversely to the optic axis. If it is transversely displaced, this manifests as an angular displacement of the collimated light after the triplet lens. A large angular displacement is undesirable due to the fact that since one of the Raman light fields propagates further, the two wavefronts that drive acceleration-sensitive Raman transitions are not parallel. Figure 1.4a shows a simulation of the wavefront distortion as a result of this transverse misalignment. This is obtained by simulating the propagation of rays corresponding to each Raman light field through the optical system. The wavefront is estimated using the slope of each ray at a distance of 43 mm from the output of the triplet lens, which corresponds to the position of the centre of the vacuum chamber. The mirror is mounted at the same distance from the centre, so the second beam propagates 129 mm. Close to the

optic axis, this distortion is approximately linear (i.e. a tilt) and it can be seen that a displacement of the fibre from the optic axis of <1 mm is sufficient to achieve the desired wavefront flatness.

Aside from a transverse displacement, it is possible that the fibre could be misaligned along the optic axis. In which case, the output beam will not be collimated. Consequently, the counter-propagating reflected rays will not be antiparallel to incoming ones. The effect of this longitudinal displacement on the Raman wavefront is shown in Figure 1.4b. Further from the optic axis the deviation in the phase of the light is greater, giving a quadratic distortion which is characteristic of a defocus. Comparing the wavefront distortion in this case, a requirement on the longitudinal misalignment of < 0.6 mm is needed for the previously specified flatness.

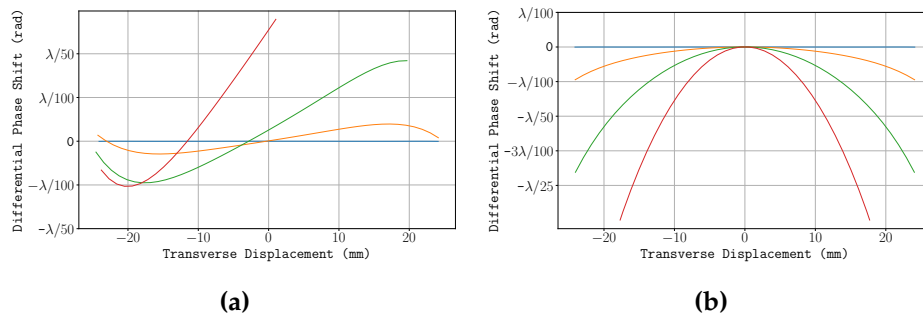


Figure 1.4: Simulated wavefront distortion for longitudinal and transverse fibre misalignment. Rays from a point source with a divergence angle corresponding to a $na!$ of 0.12 are propagated through the Raman optical system. Rays corresponding to the reflected beam are propagated further with the assumption that the mirror is perpendicular to the optic axis. The first set of rays propagates 43 mm and the second propagates 129 mm. The wavefront for each beam is calculated by taking the slope of each ray and subtracting from the slope of the central ray. The wavefront of the effective field that drives the Raman transition is the difference of these two wavefronts. (a) shows the distortion of the wavefront for a transverse misalignment of the fibre for a displacement of 0 mm (blue), 0.5 mm (orange) 1 mm (green) and 1.5 mm (red) from the front focal point. (b) shows the wavefront for longitudinal displacements of 0 mm (blue), 0.3 mm (orange) 0.6 mm (green) and 1 mm (red).

Measuring the Beam Width

To measure the waist of the beam, its reflection from a flat surface was imaged using a CCD camera. The radius of the triplet lens is smaller than the beam waist, so the beam is apertured by this lens. To take account of this aperture, the beam waist was estimated using a Taylor expansion of a Gaussian to second order:

$$\begin{aligned} I(x) &= Ae^{-\frac{(x-x_0)^2}{2w^2}} \\ &\approx A - \frac{2Ax_0^2}{w^2} + \frac{4Ax_0}{w^2} - \frac{2Ax^2}{w^2} + \mathcal{O}(x^3) \end{aligned} \quad (1.6)$$

A typical intensity profile along the horizontal and vertical camera axes is shown in Figure 1.5b. A threshold intensity value excludes contributions from pixels outside of the spatial extent of the beam. The waist was estimated using a linear least-squares fit of the intensity profile to a second-order polynomial $c_0 + c_1x + c_2x^2$, where

$$w = \left| \frac{\sqrt{c_1^2 - 4c_0c_2}}{\sqrt{2}c_2} \right| \quad (1.7)$$

A plot of the estimated beam waist over a propagation distance of 1 m is shown in Figure 1.5a. Inside the chamber each Raman beam propagates 5.25 cm and 15.75 cm, where the beam is well collimated. Along the vertical axis, the beam has a waist of around 36.9 mm. The horizontal waist is smaller because the camera was horizontally tilted from the beam's optic axis. The projection of the beam onto this axis is consistent with a horizontal tilt of 16° .

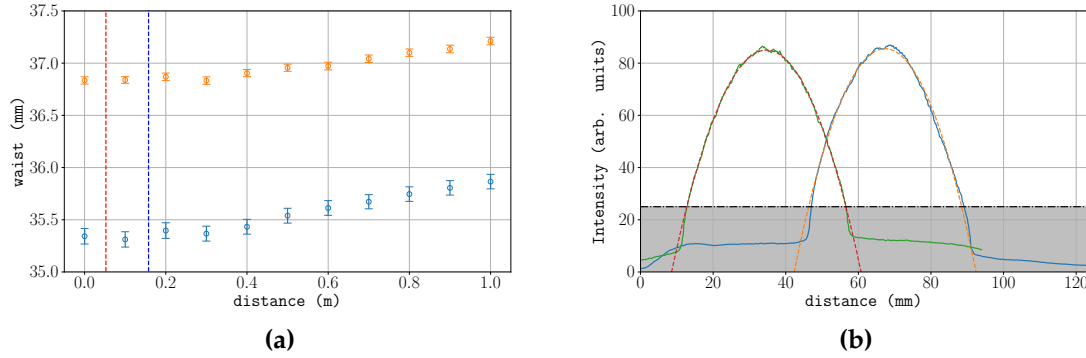


Figure 1.5: Raman beam waist measured over a distance of 1 m, shown in **(a)**. The waist along the horizontal and vertical axes are indicated in blue and orange respectively. The dashed lines indicate the approximate propagation distance of each beam at the position of the atoms. **(b)** shows the intensity profile along each axis, with the fitted parabola. The dot-dashed line is a threshold intensity value, which excludes pixels from outside the spatial extent of the beam.

1.3.3 Retro-reflection Assembly

The Raman transitions used in the interferometer are driven by counter-propagating light fields to give a large momentum transfer of $2\hbar k$ to the atoms. The two beams enter from the same fibre input, so a mirror is used to retro-reflect them. The retro-reflection assembly includes a **qwp!** to ensure that the reflected beams have the same polarisation handedness as their circularly polarised incoming counterpart.

The mirror is also manufactured by Light Machinery, and the **qwp!** is made to the same specifications as the one that circularly polarises the incoming beams. During the manufacturing process, the waveplates and mirror were polished to reduce irregularities in the thickness of each **qwp!** and the surface of the mirror. Figure 1.6 shows the variation in the thickness of the waveplate in front of the triplet lens, measured by Light Machinery using a white light interferometer. This has a standard deviation of 4.62 nm and corresponds a standard deviation of the optical path length of $8.6 \times 10^{-3} \lambda$.

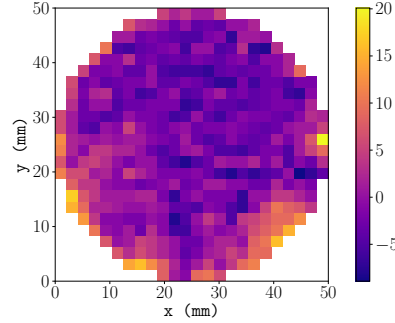


Figure 1.6: Thickness of the first **QWP**, measured by a white light interferometer. The value is given in nm as a difference from the mean thickness. The standard deviation of this thickness is 4.62 nm and a peak-to-valley (PV) of need number here. Equivalent surface data for the other **QWP** and mirror were not provided by Light Machinery, but had a PV thickness variation of 19 nm and 9 nm respectively.

The **qwp** and mirror are fixed onto the front plate of a UHV compatible MDI-HS mirror mount, manufactured by Radiant dye. The horizontal and vertical tilt of the mirror can be adjusted using two thumbscrew actuators which cause the front plate to pivot around a ball bearing. This mount is designed for high stability, but of course the alignment will still drift over time. To avoid the need to periodically open the chamber to realign the mirror, a piezo-electric stack is placed between each actuator and the front plate so that the tilt of the mirror can be adjusted externally. Each piezo-stack is connected to a high-voltage feedthrough, so that their length (and hence mirror tilt) can be finely adjusted by controlling the voltage applied across them. A control voltage ranging between 0–10 V is amplified by a controller to give an applied voltage across the piezo stack between -10–150 V. This corresponds to a travel range of 23 μm .

To understand the effect of misalignment, it is instructive to consider its effect on the effective wavevector \mathbf{k}_{eff} . As illustrated in Figure ??, if the mirror is misaligned from the incoming beam's wavevector by an angle θ , the two counter-propagating fields that drive Raman transitions have wavevectors $k_1 (1, 0)$ and $k_2 (\cos(\theta), \sin(\theta))$. $\mathbf{k}_{\text{eff}} = \mathbf{k}_1 - \mathbf{k}_2 \cos(2\theta_i)$. Fortunately, for small angular displacements, i.e. < 1 mrad, this does not greatly reduce the sensitivity to accelerations. In short, this means that

\mathbf{k}_{eff} will have a spatially varying direction. Since an atom interacting via a Raman transition picks up a phase $\phi = \mathbf{k}_{\text{eff}} \cdot \mathbf{x}$, atoms travelling along different trajectories will accumulate different phases due to the spatial variation of \mathbf{k}_{eff} . Across the atom ensemble, this leads to a dephasing and consequently, a loss of interferometer fringe visibility [3]

In-Situ Alignment and Optimisation

After mounting the Raman optical system inside the chamber, the mirror had to be aligned to retro-reflect the light. When the mirror is close to perpendicular to the light's wavevector, some of the power in the reflected beam couples back into the fibre. In principle, this power is maximised when the mirror is exactly perpendicular so maximising this power is a useful technique to align the mirror. A 99:1 fibre splitter was used to couple light into the chamber, which provided a means to measure the back-reflected power without needing any free-space optics. This was set up so that 99% of the incoming light entered the chamber, with the other 1% coupled into the corresponding output port. Due to the fact that a beam-splitter acts reversibly, 1% of the back-reflected light which couples into vacuum fibre exits the fibre-splitter on the other input port. Therefore, the power at this output was used to indirectly measure the alignment of the mirror.

Since the travel range of the piezo stacks does not cover the full motional range of the mirror mount, the mirror initially had to be manually aligned using the thumb-screw actuators. Once installed, the lack of direct access to optical system meant that conventional methods to coarsely align the mirror, such as observing the location of the reflected beam's focus, were not feasible. Rather than carry out the somewhat tedious job of systematically adjusting each thumbscrew until the mirror was aligned, an automatic routine was devised to do this. This was carried out using a pair of

bipolar stepper motors that each rotated a ball driver inserted into the head of each thumbscrew. The revolution of these motors was controlled using an arduino micro-controller, which communicated to the computer using a serial interface. The motors rotated by $0.9^\circ/\text{step}$, which corresponds to a tilt of the mirror by $18.1 \mu\text{rad}$. This is smaller than the 0.67 mrad angular displacement that the piezo stack could provide, but the slow execution speed of the motor control meant that it was more practical to use a combination of the motors and piezos to systematically scan through the tilt of the mirror mount. **huge find out how big spot size was .**

Using this method, the mirror mount was aligned so that the the maximum of the back-reflected power was reachable with the piezo stacks. Of course, it was foreseeable that the mirror would need to be periodically realigned, which would require another systematic iteration through the voltages applied to each piezo stack. Given that this search was quite time consuming, it was not a practical way to maintain alignment. To improve upon this, an optimisation method using the Nelder-Mead simplex algorithm [2] was implemented. This method is suitable for optimising multidimensional functions and has been used to demonstrate the automatic alignment of a fibre with up to 6 degrees of freedom [5]. In general terms, this algorithm aims to optimise the value of an objective function (in this instance, the optical power measured as a voltage by a photodiode) by sampling the function at various locations. For n parameters, a set of $n - 1$ points distributed randomly across the parameter space are chosen as the initial simplex. These are sorted in decreasing order of the value of the objective function and the algorithm proceeds by performing geometric transformations on this simplex, by sequentially reflecting, expanding and contracting this simplex. Each step starts with a reflection about the line between the two greatest values. The coordinates of the simplex are updated if the function has a greater value at the location given by one of these transformations, until the algorithm converges on a maximum value. As with many optimisation algorithms, the Nelder-Mead method has the potential to

converge on a local optimum, but this is alleviated by expanding the simplex to look for more optimal values. The termination of the algorithm was decided by using the standard deviation of the last 5 values. Empirically, it was found that terminating when the standard deviation was less than $10\text{ }\mu\text{V}$ resulted in stable performance of the algorithm, even when the signal-to-noise ratio of the measured voltage was poor. An example of this algorithm aligning the mirror mount is presented in Figure 1.7. To verify that the converged value was optimal, a systematic scan of the piezo stack control voltages in the region around this value was also carried out. In this case, the algorithm converged on a local maximum, but one that greatly enhanced the coupling efficiency of the reflected light back into the fibre. The difference in the piezo control voltages from their optimal values corresponds to a tilt of the mirror mount along the horizontal and vertical axis of less than $13\text{ }\mu\text{rad}$.

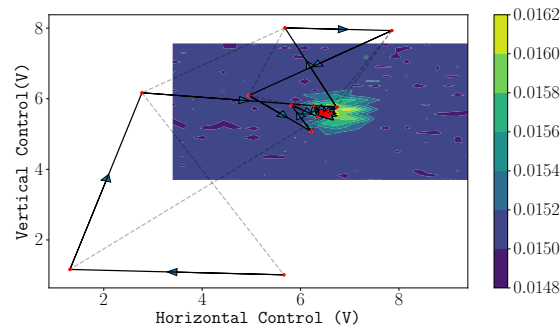


Figure 1.7: Automatic mirror alignment using the Nelder-Mead simplex algorithm. This procedure starts by randomly selecting three pairs of control voltages for the horizontal and vertical piezo stacks. At each co-ordinate, the back-reflected power is measured. The algorithm proceeds by geometrically transforming the simplex using reflections, expansions and contractions, and updating the simplex using this new co-ordinate if the power measured is greater than the current lowest value. The algorithm uses the standard deviation of the last 5 values as a check for convergence. In this case, it terminates once the standard deviation is smaller than $10\text{ }\mu\text{V}$. The shaded lines indicate the simplex bounded by the three co-ordinates at each iteration, whose area reduces as the algorithm converges on the optimum value. A scan of the piezo control voltages close to the optimum is also plotted. The irregular shape of the measured power is a result of a hysteresis effect when the horizontal control voltage was changed from its maximum value to the minimum. Even with a low signal-to-noise ratio, the algorithm converged on a value close to the optimum. This resulted in a misalignment of less than $13\text{ }\mu\text{rad}$ along both axes.

1.3.4 The Mechanical Accelerometer

The periodic interferometer signal means that the interferometer phase is only proportional to acceleration over one fringe spacing $\Delta a = \frac{\pi}{k_{\text{eff}} T^2}$. Furthermore, the fringe spacing is inversely proportional to T^2 so there is a trade-off between dynamic range and sensitivity. These problems can be addressed by making use of a mechanical accelerometer mounted onto the back of the retro-reflecting mirror to form a hybrid system [Lautier2014]. The accelerometer determines the acceleration up to the fringe spacing and the interferometer measures the acceleration more precisely. The accelerometer also measures the vibrations of the retro-reflecting mirror, so it can be used to filter the effects of vibration noise on the interferometer signal. This is discussed in more detail in Section 1.8.1. This hybridisation scheme has been used in measurements of gravity in high noise environments such as the centre of Paris [Merlet2009] and in parabolic aircraft flights [Geiger2011a, Barrett2016a].

The accelerometer is a navigation-grade AI-Q-2010 manufactured by *Innalabs*. This particular device was chosen because its specified intrinsic noise was $<7 \mu\text{g}$ in the 0-100Hz! (Hz!) bandwidth. For a pulse separation $T = 25 \text{ ms}$, the fringe spacing is $31.2 \mu\text{g}$ so it is sensitive enough to measure the acceleration to within one fringe. A schematic of this device is shown in Figure 1.8. It operates using a quartz pendulum which is free to move about one axis [1]. Under an acceleration, the deflection of the pendulum is capacitively detected. A servo loop circuit drives a current through the coils to restore the position of the pendulum. This current is directly proportional to the acceleration of the pendulum. This model has a nominal scale factor of $1.235\,976 \text{ mA g}^{-1}$. The acceleration is measured using a load resistance of $6 \text{ k}\Omega$ to give an output voltage of 7.56 V g^{-1} .

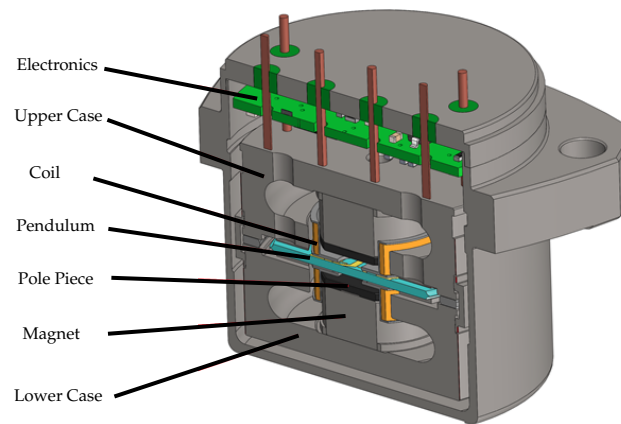


Figure 1.8: Cross-section of the Innalabs AI-Q-2010 accelerometer.

Accelerometer Noise Spectrum

- Plot noise spectrum
- Explain how it differs when the table is floated

1.4 The M-Squared Laser System

- M2 laser diagram
- Real-time communication
- Describe how it controls the frequency and phase of the two lasers
- DCS

This section describes the laser system manufactured by *M-Squared Lasers*, which is used to drive Raman transitions. An overview of the laser system can be found in Section 1.4.1, which includes the techniques used to externally communicate with the laser's ICE-BLOC control modules. The control of the frequency and phase-lock is then described in Section 1.4.2. Finally, this section concludes in Section ?? with a description of the module used to control the output of the laser in real-time.

1.4.1 Laser System Overview

This system contains two Solstis lasers which generate laser light by pumping a Ti-sapphire crystal housed inside a resonator. The output light frequency is controlled using piezo-electric stacks to adjust the resonator length. A schematic diagram of this laser system is given in Figure 1.9. Each laser is seeded using a *Lighthouse Photonics* Sprout laser to generate light around 780 nm. The first laser acts as the master whose frequency is fixed. The second is slaved to this using a phase-locked loop to keep their beat frequency and relative phase constant. The two beams are mixed on a **pbs!** (**pbs!**), so that they are orthogonally polarised. Two **aoms!** (**aoms!**) control the output power. A planned upgrade for this system will have multiple output ports for the Raman light, which will require independent control.

The system contains 4 ICE-BLOC modules which implement various types of control. The first two (one for each Solstis) are used to stabilise the output power of each laser by feeding back to the corresponding Sprout laser. They are also used to coarsely adjust the output frequency using a *HighFinesse* wavemeter. The third is used for the **pll!** (**pll!**) and feeds-back onto the slave laser to control both the frequency and phase of the optical beat-note between the two lasers. The final ICE-BLOC, referred to as the DCS module, is used to control the lasers in real-time during the experiment.

External ICE-BLOC Control

The ICE-BLOC modules are able to communicate with each other using an ethernet hub. Another computer connected to this network is able to control them by accessing a webpage that each module hosts. These webpages control the ICE-BLOCs by sending structured JSON messages. This graphical interface can be bypassed by directly communicating these messages. This is done using MOTMaster so that various param-

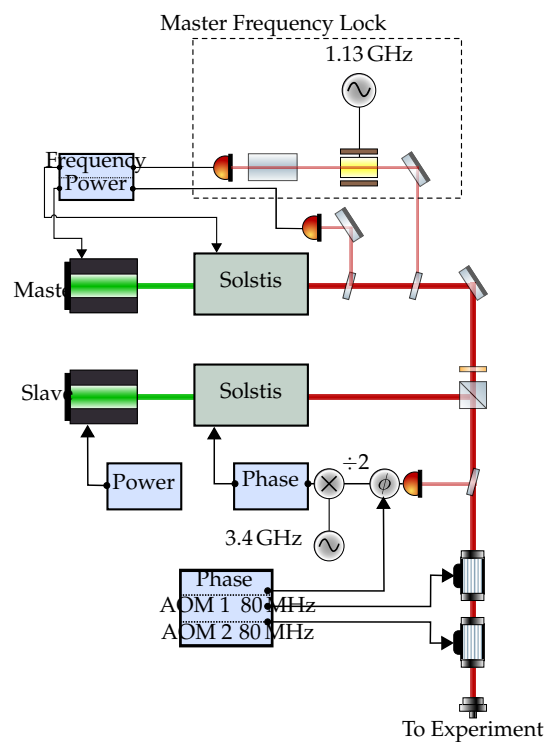


Figure 1.9: Schematic Diagram of the M-Squared laser system. Two Solstis lasers provide the two Raman frequencies, which are fibre coupled onto the orthogonal axes of a **pm!** fibre. Control of the power, frequency and phase as required to drive Raman transitions is handled by the four ICE-BLOC modules indicated in blue. Further detail of this control is given in the text.

eters, such as the frequency and phase of the Raman beat-note, can be automatically varied between each experiment cycle.

1.4.2 Frequency and Phase Control

Master Lock

The frequency of the master laser is stabilised using saturated absorption spectroscopy in a rubidium vapour cell. Part of the beam is picked off and modulated by an **eom!** (**eom!**). The positive frequency sideband is used to lock the master laser to the 2,3 crossover feature. In effect, this means that the modulation frequency of the **eom!** sets the one-photon detuning of the Raman transition. The modulation frequency is set so that the master laser frequency is 1.13 GHz below the $|F = 2\rangle \rightarrow |F' = 3\rangle$ transition.

Frequency and Phase Lock

The optical beat-note between the two lasers is measured using a fast photodiode. The signal from this is used in a phase-locked loop to fix the relative phase between the two lasers. A frequency divider halves the frequency of the signal before comparing it to a **vco!** (**vco!**) of around 3.4 GHz. This creates an error signal which used to control both the frequency and phase of the beat-note by feeding back to the slave laser Solstis. The relative phase between the two lasers is adjusted using an analogue phase shifter and the frequency difference is controlled by tuning the **vco!** frequency.

The beat-frequency of the Raman lasers can be chirped by triggering a ramp of the control voltage to the **vco!**. For chirp rates of lower than 24 MHz s^{-1} , the phase-lock is able to keep the beat-note phase-coherent during the chirp.

1.4.3 The DCS Module

The DCS module is used to control the output of the lasers during the experiment. It uses an on-board **DDS!** (**DDS!**) to synthesise the 80 MHz driving frequencies for each **aom!** (**aom!**). The majority of the control is done using an **fpga!** (**fpga!**) that synthesises a timed sequence of analogue and digital voltage waveforms. An example of a sequence created using the DCS web interface is shown in Figure 1.10. The sequence is segmented into individual steps and each channel can be separately configured, much like the MOTMaster user interface.

This module is used to control the amplitude, frequency and phase of each Raman pulse. The pulse amplitude is shaped using an analogue voltage to control the power of the RF frequency. This has been calibrated so that the pulse can be shaped to produce a square, Gaussian or Blackman amplitude envelope. A frequency chirp is optionally triggered by sending a digital pulse to the **p11!** ICE-BLOC.

The synthesiser can be configured to run continuously, or to wait at a chosen timestep for an external trigger. It can also iterate through a set number of parameters, such as timestep duration or phase shift by re-building the sequence after each cycle.

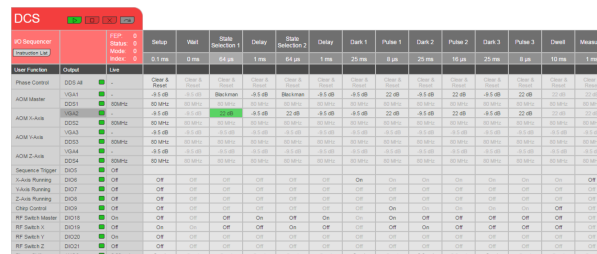


Figure 1.10: DCS module user interface. The sequence is synthesised from individual steps, The parameters of each Raman laser pulse can be configured independently.

1.5 Atom Detection

- Photodiode system - diagram
- Detection sequence - diagram
- Statistical analysis to estimate phase from measured voltages
- Simulate detection curves?

This section describes the methods used to measure the number of atoms in each hyperfine ground state. It begins with a presentation of the other optical components used to detect the atoms by driving σ^+ transitions in Section 1.5.2. The sequence of light pulses used to measure the number of atoms is then given in Section 1.5.2. This concludes with a discussion on converting the measured photodiode signals into atom number and interferometer phase.

1.5.1 Optical Setup

A precise measurement of the number of atoms requires that the atom shot noise is the dominant source of uncertainty in the measurement. The CCD used in previous stages of the experiment is not sensitive enough for this as there is a significant amount of noise in reading out the charge collected at each pixel. Instead, a more sensitive photodiode is used to detect the atoms. With a suitably high bandwidth, the readout time is much faster than the CCD as well, so that the atoms can be detected well before they fall out of the field of view.

A diagram of the setup used to detect the atoms is given in Figure 1.12. It is a triplet system which uses lenses with focal lengths 150 mm, 75 mm and 60 mm in order from the atoms to the photodiode. A ray-tracing simulation of the optical system

indicates spherical aberrations on the image. This is caused by the third lens, which was added to shorten the back focal length. The photodiode used is a *Femto LCA-S-400K-SI*, which has a trans-impedance amplifier with a bandwidth of 400 kHz and a photo-sensitive area with a diameter of 3 mm.

Photodiode Calibration

A calibration of the output voltage for an input collimated beam is shown in Figure ?? . This gives a conversion factor of $1.84 \times 10^6 \text{ V W}^{-1}$.

1.5.2 Detection using σ^+ transitions

The atoms are detected using resonance fluorescence from two of the circularly polarised **mot!** beams. A bias field polarises the atoms along the \vec{z} axis, so that the light drives both σ^+ and σ^- transitions. Each Zeeman state has a different scattering rate, which must be accounted for to calculate the number of atoms. This can be simplified by flipping the handed-ness of one of the \vec{z} **mot!** beams using a liquid-crystal **hwp!** (**hwp!**), so that both beams drive σ^+ transitions. Now, the atoms are optically pumped into $|2, 2\rangle$ and cycle on the $|2, 2\rangle \rightarrow |3, 3\rangle$ transition. Only this scattering rate is required to determine the number of atoms.

Figure 1.11 shows the setup used to invert the polarisation of one **mot!** beam for detection. The liquid-crystal waveplate is an electro-optical device whose birefringence changes when an ac voltage is applied across it. The waveplate is placed at the output of the downward-propagating (\vec{z}_-) collimator.

Figure 1.11: Scheme for detection by driving σ^+ transitions. A liquid-crystal waveplate flips the handedness of the \vec{z}_- beam. The atoms then fluoresce on the $|2,2\rangle \rightarrow |4,3\rangle$ cycling transition

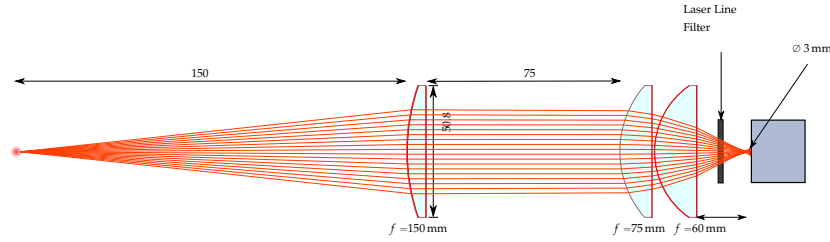


Figure 1.12: Optical setup for photodiode detection. A triplet lens system focuses light from radiated from the atoms onto a photodiode. This is mounted using a translation stage to position the photodiode at the back focal point.

Detection Sequence

detection volume for a longer period of time. The intensity of the light is reduced to around I_{sat} , so that the scattering rate per atom is approximately linear. The photodiode is triggered to start at the first Dwell time. The cooling light is first switched on, so that only atoms in $|F = 2\rangle$ scatter light. After this, the repump is switched on, so that atoms in $|F = 1\rangle$ are optically pumped into $|F = 2\rangle$ and all the atoms scatter light. This repump light is a sideband of the cooling laser, so the total output is increased to ensure that the intensity of the cooling light remains constant. Each detection step lasts 250 μs , but the first 50 μs is discarded to allow time for the intensity to stabilise and for optical pumping into $|F = 2\rangle$. The atoms are then blown away by switching off one of the detection beams before the sequence is repeated to collect a background signal.

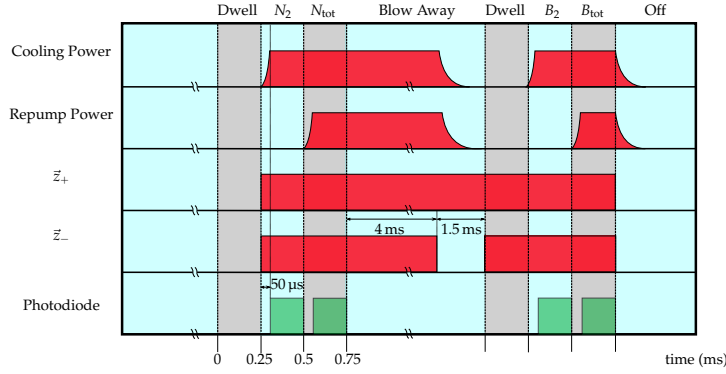


Figure 1.13: Timing diagram for state detection. Atoms in $|F = 2\rangle$ are detected before the repump light pumps those in $|F = 1\rangle$, so they are detected as well. A background light measurement for each step is also taken.

1.5.3 Measuring the Occupation Probability

The occupation probability is obtained by measuring the proportion of atoms in each hyperfine ground state. The number of atoms n_{at} that scatter light on the cycling transition is proportional to the photodiode voltage U_{pd} as follows

$$\begin{aligned} U_{\text{pd}} &= \eta R_{\text{sc}}(I, \Delta) n_{\text{at}} \hbar \omega G \\ &= \alpha \eta R_{\text{sc}}(I, \Delta) n_{\text{at}} \end{aligned} \quad (1.8)$$

where $\eta = \Omega/4\pi$ is the fractional solid angle subtended by the collection optics, $\hbar \omega = 1.6 \text{ eV}$ is the photon energy, R_{sc} is the scattering rate defined in equation (??) and G is the photodiode conversion gain. The probability of an atom occupying $|F = 2\rangle$ is calculated as follows

$$P_{|F=2\rangle} = \frac{N_2 - B_2}{N_{\text{Tot}} - B_{\text{Tot}}} \quad (1.9)$$

where N and B denote the signal and background measurements, respectively. Subtracting the background signal from each measurement removes the bias that arises from detecting light not scattered by the atoms. Under a constant scattering rate and

collection efficiency, the scaling factor between atom number and photodiode voltage cancels in equation (1.9). The interferometer phase Φ is determined from equation (1.9) using

$$P_{|F=2\rangle} = P_0 + \frac{C}{2} \cos(\Phi/2)^2 \quad (1.10)$$

where

1.5.4 Sources of Detection Noise

- Contributions to detection noise
- Calibrating detector
- Atom-equivalent noise

Each measurement of the number of atoms has a systematic uncertainty due to random processes that influence the detection signal. This error propagates to given an uncertainty and the interferometer phase and hence, acceleration. Characterisation of these noise sources is required to understand their effects on the sensitivity to accelerations. These both have shot noise fluctuations which introduce an uncertainty on the interferometer phase. Finally, there is also technical noise in the detector itself. The contribution from each source can be understood using their power spectral densities.

Atom and Photon Shot Noise

The discrete nature and the fact that atoms are loaded into the experiment and scatter photons at a constant rate mean that the statistics on the number of atoms and photons are well-described by Poisson distributions. Therefore, the number of atoms in

the interferometer and number of photons arriving at the detector have shot noise fluctuations with variances given by their mean values. From equation (1.8), these are related to an equivalent output voltage as follows

$$\sigma_{\text{at},v}^2 = \alpha^2 \eta^2 R_{\text{sc}}^2 n_{\text{at}} \quad (1.11)$$

$$\sigma_{\text{p},v}^2 = \alpha^2 \eta R_{\text{sc}} n_{\text{at}} \quad (1.12)$$

where $\sigma_{\text{at},v}$ dominates, provided at least one photon per atom is detected. For a large number of particles, shot noise approaches a Gaussian distribution, which has a uniform power spectral density. However, the finite detection time acts as a low-pass filter by limiting the influence of frequency components above the sampling frequency. In the time domain, the signal is convolved with a rectangular pulse of a characteristic time τ , so the power spectral density is a product of the individual power spectral densities

$$S(f) = 2S_0 \left(\frac{\sin(\pi f \tau)}{\pi f \tau} \right)^2 \quad (1.13)$$

where S_0 is the one-sided power spectral density of the shot noise component. From the Wiener-Khinchin theorem, the variance is equal to the integral of the power spectral density, so

$$S_0 = \sigma_{\text{i},v}^2 \tau \quad (1.14)$$

For shorter detection times, this has the effect of aliasing high-frequency noise into the lower-frequency components.

Photodiode Technical Noise

A further source of noise is technical noise in the photodiode and amplifier. This arises from multiple electronic processes – such as Johnson noise and shot noise in the current – but it is not necessary to consider them independently in the following discussion. Since this technical noise does not depend on the number of atoms, it adds a systematic uncertainty to the measured interferometer phase. The technical noise of the photodiode and amplifier is a source of uncertainty in the output voltage. The nep! (nep!) is useful in determining the noise from the photodiode when the signal is averaged over a given integration time. A plot of the noise-equivalent power of the photodiode is shown in Figure ?? taken with a sampling frequency of 200 kHz. The photodiode was covered and the output voltage was sampled for 2 s. The power sp has been calculated using Welch's method [4]. This partitions the data before calculating the Fourier transform of each subset and taking the average. This has the effect of reducing the variance in the estimated power spectrum at the expense of reducing the frequency resolution. The nep! is then given by

$$NP(f) = \frac{1}{GR} S(f) \quad (1.15)$$

where $G = 1 \times 10^7 \text{ V A}^{-1}$ is the transimpedance Gain, $R = 0.54 \text{ A W}^{-1}$ is the responsivity of the photodiode and S is the amplitude spectral density.

1.6 Individual Pulse Characterisation

1.6.1 Raman Spectrum

- Raman transition spectrum identifying Doppler width

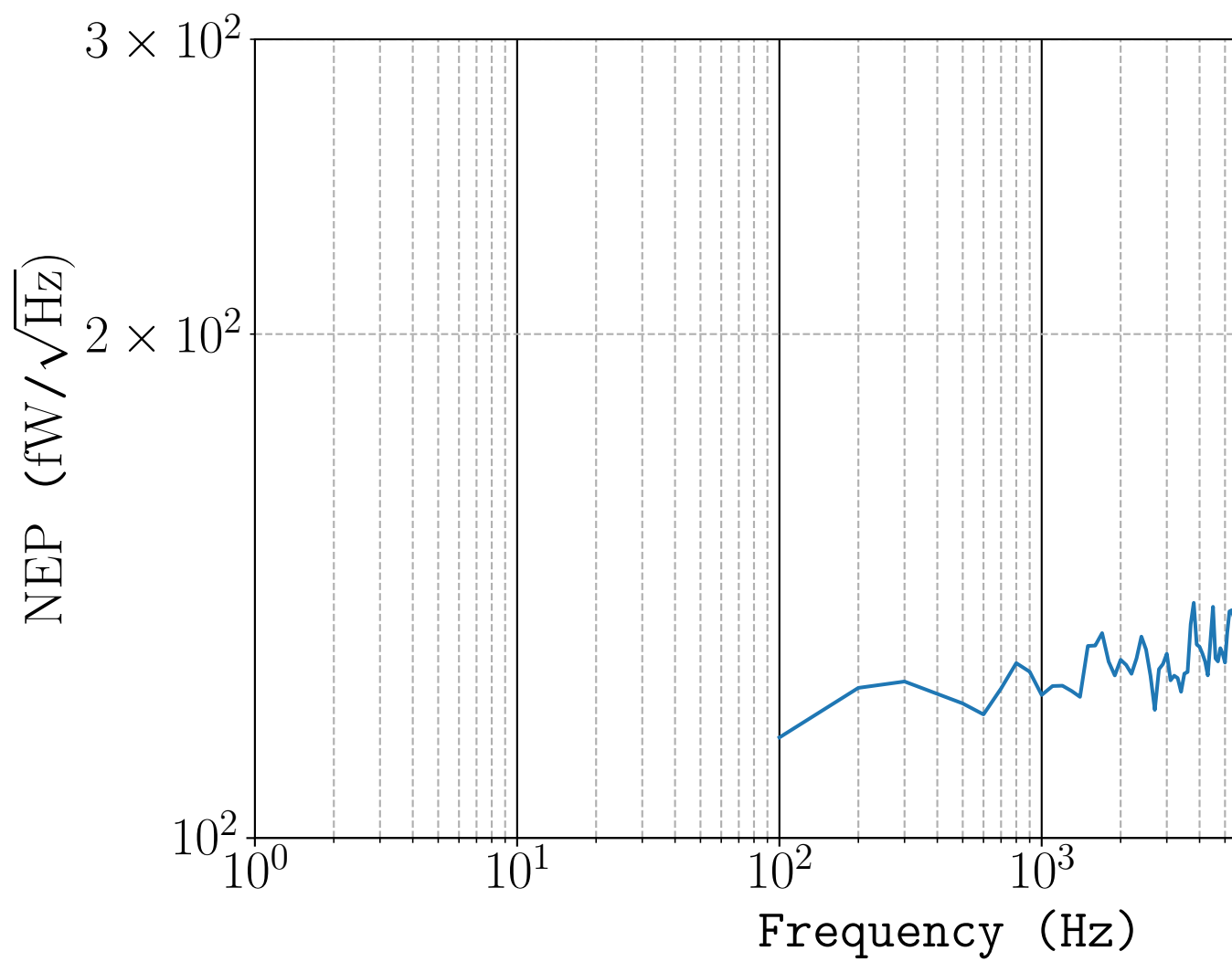


Figure 1.14: Power spectral density of the photodiode output voltage sampled for 2 s at a rate of

- Explain the large co-propagating peak
- Asymmetry between $\pm k$

1.6.2 Velocity-Selective Pulse

- Spectrum after velocity selection
- How does linewidth of Raman pulse affect final velocity distribution?
- Why do we need this?
- Final Doppler width

1.6.3 Interferometer Pulses

- Pulse characterisation for each pulse
- Fit to dephasing

1.7 Three-Pulse Atom Interference

1.7.1 Fringe Contrast vs. Launch Trajectory

1.8 Measuring Accelerations

1.8.1 Vibration Sensitivity

The mirror defines an inertial frame of reference – the interferometer measures acceleration of the atoms relative to the acceleration of the mirror. Vibrations of the mirror introduce a component of the interferometer phase which is independent of acceleration. This vibration-induced phase can be accounted for by mounting the accelerometer onto the back of the mirror. During the interferometer, the accelerometer measures the acceleration of the mirror.

1.9 Sensitivity

1.9.1 Loading Rate

A fundamental limit to the uncertainty on the number of atoms is given by the statistics of the total number of atoms in the experiment. For short loading times, atoms are loaded into the **mot!** at a constant rate, so the total number of atoms after the experiment follows a Poisson dis

1.9.2 Detection Noise

The

1.9.3 Vibrations

Bibliography

- [1] S.A. Foote and D.B. Grindeland. “Model QA3000 Q-Flex accelerometer high performance test results”. In: *IEEE Aerospace and Electronic Systems Magazine* 7.6 (1992), pp. 59–67. ISSN: 0885-8985. DOI: [10.1109/62.145120](https://doi.org/10.1109/62.145120).
- [2] J. A. Nelder and R. Mead. “A Simplex Method for Function Minimization”. In: *The Computer Journal* 7.4 (1965), pp. 308–313. ISSN: 0010-4620. DOI: [10.1093/comjnl/7.4.308](https://doi.org/10.1093/comjnl/7.4.308).
- [3] G Tackmann et al. “Self-alignment of a compact large-area atomic Sagnac interferometer”. In: *New Journal of Physics* 14.1 (2012), p. 015002. ISSN: 1367-2630. DOI: [10.1088/1367-2630/14/1/015002](https://doi.org/10.1088/1367-2630/14/1/015002).
- [4] P. Welch. “The use of fast Fourier transform for the estimation of power spectra: A method based on time averaging over short, modified periodograms”. In: *IEEE Transactions on Audio and Electroacoustics* 15.2 (1967), pp. 70–73. ISSN: 0018-9278. DOI: [10.1109/TAU.1967.1161901](https://doi.org/10.1109/TAU.1967.1161901).
- [5] R. Zhang and F.G. Shi. “A Novel Algorithm for Fiber-Optic Alignment Automation”. In: *IEEE Transactions on Advanced Packaging* 27.1 (2004), pp. 173–178. ISSN: 1521-3323. DOI: [10.1109/TADVP.2004.825434](https://doi.org/10.1109/TADVP.2004.825434).

